

The computation aspects of the equivalent-layer technique: review and perspective

Diego Takahashi^{1,*}, André L. A. Reis², Vanderlei C. Oliveira Jr.¹ and Valéria C. F. Barbosa¹

¹*Observatório Nacional, Department of Geophysics, Rio de Janeiro, Brasil*

²*Universidade do Estado do Rio de Janeiro, Department of Applied Geology, Rio de Janeiro, Brasil*

Correspondence*: Valéria C.F. Barbosa
valcris@on.br

2 ABSTRACT

3 Equivalent-layer technique is a powerful tool for processing potential-field data in the space
4 domain. However, the greatest hindrance for using the equivalent-layer technique is its high
5 computational cost for processing massive data sets. The large amount of computer memory
6 usage to store the full sensitivity matrix combined with the computational time required for matrix-
7 vector multiplications and to solve the resulting linear system, are the main drawbacks that made
8 unfeasible the use of the equivalent-layer technique for a long time. More recently, the advances in
9 computational power propelled the development of methods to overcome the heavy computational
10 cost associated with the equivalent-layer technique. We present a comprehensive review of the
11 computation aspects concerning the equivalent-layer technique addressing how previous works
12 have been dealt with the computational cost of this technique. Historically, the high computational
13 cost of the equivalent-layer technique has been overcome by using a variety of strategies such as:
14 moving data-window scheme, equivalent data concept, wavelet compression, lower-dimensional
15 subspace, quadtree discretization, reparametrization of the equivalent layer by a piecewise-
16 polynomial function, iterative scheme without solving a system of linear equations and the
17 convolutional equivalent layer using the concept of block-Toeplitz Toeplitz-block (BTTB) matrices.
18 We compute the number of floating-point operations of some of these strategies adopted in the
19 equivalent layer technique to show their effectiveness in reducing the computational demand.
20 Numerically, we also address the stability of some of these strategies used in the equivalent
21 layer technique by comparing with the stability via the classic equivalent-layer technique with the
22 zeroth-order Tikhonov regularization.

23 **Keywords:** equivalent layer, gravimetry, fast algorithms, computational cost, stability analysis

1 INTRODUCTION

In accord with potential theory, a continuous potential-field data (gravity and magnetic data) produced by any source can be exactly reproduced by a continuous and infinite 2D physical-property surface distribution that is called the equivalent layer. The equivalent layer is a mathematical solution of Laplace's equation in the source-free region with the observed potential-field data as the Dirichlet boundary condition (Kellogg, 1929). Grounded on well-established potential theory, the equivalent-layer technique has been used by exploration geophysicists for processing potential-field data since the late 1960s (Dampney, 1969).

Although there was always a great demand for gravity and magnetic data processing, the equivalent-layer technique has not been massively used. This occurs because its high computational cost makes the equivalent-layer technique computationally inefficient for processing massive data sets. In the classic equivalent-layer technique, the continuous problem of the equivalent layer involving integrals is approximated by a discrete form of the equivalent layer. First, a discrete and finite set of equivalent sources (point masses, prisms, magnetic dipoles, doublets) is arranged in a layer with finite horizontal dimensions and located below the observation surface. Next, a linear system of equations is set up with a large and full sensitivity matrix. Then, a regularized linear inverse problem is solved to estimate the physical property of each equivalent source within the discrete equivalent layer subject to fitting a discrete set of potential-field observations. Finally, the estimated physical-property distribution within the equivalent layer is used to accomplish the desired processing of the potential-field data (e.g., interpolation, upward/downward continuation, reduction to the pole). The latter step is done by multiplying the matrix of Green's functions associated with the desired transformation by the estimated physical-property distribution.

Beginning in the late 1980s, the equivalent-layer techniques computationally efficient have arose. To our knowledge, the first method towards improving the efficiency was proposed by Leão and Silva (1989) who used an overlapping moving-window scheme spanning the data set. The strategy adopted in Leão and Silva (1989) involves solving several smaller, regularized linear inverse problems instead of one large problem. This strategy uses a small data window and distributes equivalent sources on a small regular grid at a constant depth located below the data surface. Leão and Silva (1989) ensure that sources window extends beyond the boundaries of the data window. For each position of the data window, this scheme consists in computing the processed field at the center of the data window only and the next estimates of the processed field are obtained by shifting the data window across the entire dataset. Recently, Soler and Uieda (2021) developed a computational approach to increase the efficiency of the equivalent-layer technique by combining two strategies. The first one — the block-averaging source locations — reduces the model parameters and the second strategy — the gradient-boosted algorithm — reduces the size of the linear system to be solved by fitting the equivalent source model iteratively along overlapping windows. Notice that the equivalent-layer strategy of using a moving-window scheme either in Leão and Silva (1989) or in Soler and Uieda (2021) is similar to discrete convolution.

In another approach to reduce computational workload of the equivalent-layer technique Mendonça and Silva (1994) developed an iterative procedure by incorporating one data point at a time and thus selecting a smaller data set. This strategy adopted by Mendonça and Silva (1994) is known as 'equivalent data concept'. Li and Oldenburg (2010) transformed the full sensitivity matrix into a sparse one using the compression of the coefficient matrix via wavelet transforms based on the orthonormal compactly supported wavelets. For jointly processing the components of gravity-gradient data using the equivalent-source processing, Barnes and Lumley (2011) applied the quadtree model discretization to generate a sparse linear system of equations. Davis and Li (2011) adaptively discretized the model (quadtree model discretization) based on localized anomalies and used wavelet transforms to reduce, reordered the model parameters (Hilbert

space-filling curves) and compressed each row of the sensitivity matrix of the reordered parameter set (wavelet transforms). By using the subspace method, Mendonça (2020) reduced the dimension of the linear system of equations to be solved in the equivalent-layer technique. The subspace bases span the parameter-model space and they are constructed by applying the singular value decomposition to the matrix containing the gridded data. These strategies followed by Li and Oldenburg (2010), Barnes and Lumley (2011), Davis and Li (2011) and Mendonça (2020) may be grouped into the strategy of compression approaches to solve large linear system of equations.

Following the strategy of reparametrization of the equivalent layer, Oliveira Jr. et al. (2013) reduced the model parameters by approximating the equivalent-source layer by a piecewise-polynomial function defined on a set of user-defined small equivalent-source windows. The estimated parameters are the polynomial coefficients for each window and they are much smaller than the original number of equivalent sources. Siqueira et al. (2017) developed an iterative solution where the sensitivity matrix is transformed into a diagonal matrix with constant terms through the use of the 'excess mass criterion' and of the positive correlation between the observed gravity data and the masses on the equivalent layer. Jirigalatu and Ebbing (2019) combined the Gauss-fast Fourier transform (FFT) with Landweber's algorithm and proposed a fast equivalent-layer technique for jointly processing two-components of the gravity-gradient data. The Landweber's algorithm has some similarities with gradient-descent algorithm. The strategies worked out by Siqueira et al. (2017) and Jirigalatu and Ebbing (2019) avoid calculating the Hessian matrix and solving linear system of equations.

Recently, Takahashi et al. (2020, 2022), developed fast and effective equivalent-layer techniques for processing, respectively, gravity and magnetic data by modifying the forward modeling to estimate the physical-property distribution over the layer through a 2D discrete convolution that can be efficiently computed via 2D FFT. These methods took advantage of the Block-Toeplitz Toeplitz-block (BTTB) structure of the sensitivity matrices, allowing them to be calculated by using only their first column. In practice, the forward modeling uses a single equivalent source, which significantly reduces the required RAM memory. Takahashi et al. (2020, 2022) employed the strategy of the convolutional equivalent layer using the concept of BTTB matrices.

Here, we present a comprehensive review of diverse strategies to solve the linear system of the equivalent layer alongside an analysis of the computational cost and stability of these strategies. To do this analysis we are using the floating-point operations count to evaluate the performance of each method and the sensitivity to noise of linear systems as a comparison parameter to stability. A potential field transformation will also be used to evaluate the quality of the equivalent sources estimation results.

2 THE EQUIVALENT-LAYER TECHNIQUE

99 2.1 Fundamentals

100 Consider a set of N potential-field observations (gravity or magnetic data) $d_i^o(x_i, y_i, z_i)$, $i = 1, \dots, N$,
 101 at the i th observation point (x_i, y_i, z_i) of a Cartesian coordinate system with x -, y - and z -axis pointing to
 102 north, east and down, respectively. Physically, the discrete set of potential-field observations is produced by
 103 a unknown source distribution in the subsurface. Mathematically, it represents a discrete set of a harmonic
 104 function.

105 A standard way to deal with the classical equivalent-layer technique is approximate the observed potential-
 106 field data by the predicted data, which in turn are produced by a fictitious layer of sources, called equivalent
 107 layer. The equivalent layer is located below the observation surface, at depth z_0 ($z_0 > z_i$), and with finite
 108 horizontal dimensions being composed by a finite discrete set of equivalent sources (e.g., point masses,
 109 dipoles, or prisms). Mathematically, this approximation can be written in matrix notation as

$$\mathbf{d} = \mathbf{A}\mathbf{p}, \quad (1)$$

110 where \mathbf{d} is an N -dimensional predicted data vector whose i th element, $d_i(x_i, y_i, z_i)$, $i = 1, \dots, N$, is the
 111 predicted potential-field observation, \mathbf{p} is an M -dimensional parameter vector whose j th element p_j can be
 112 a physical property of the j th equivalent source and \mathbf{A} is the $N \times M$ sensitivity matrix whose ij th element
 113 a_{ij} is a harmonic function.

114 2.2 Computational strategies

115 The classical equivalent-layer technique consists of estimating the parameter vector \mathbf{p} from the N -
 116 dimensional observed data vector \mathbf{d}^o whose i th element is defined as the $d_i^o(x_i, y_i, z_i)$, $i = 1, \dots, N$.
 117 Usually, this estimate can be obtained by a regularized least-squares solution. The estimated parameter
 118 is stable, fits the observed data and can be used to yield a desired linear transformation of the data, such
 119 as interpolation, upward (or downward) continuation, reduction to the pole, joint processing of gravity
 120 gradient data and more. Mathematically, the desired linear transformation of the data can be obtained by

$$\hat{\mathbf{t}} = \mathbf{T}\mathbf{p}^*, \quad (2)$$

121 where $\hat{\mathbf{t}}$ is an N -dimensional transformed data vector, \mathbf{p}^* is an M -dimensional estimated parameter vector
 122 and \mathbf{T} is the $N \times M$ matrix of Green's functions whose ij th element is the transformed field at the i th
 123 observation point produced by the j th equivalent source.

124 The biggest hurdle to use the classical equivalent-layer technique is the computational complexity
 125 to handle large datasets because the sensitivity matrix \mathbf{A} (equation 1) is dense. Usually, the estimated
 126 parameter vector \mathbf{p}^* requires to solve a large-scale linear inversion which in turn means to deal with
 127 some obstacles concerning large computational cost: i) the large computer memory to store large and full
 128 matrices; ii) the long computation time to multiply a matrix by a vector; and iii) the long computation time
 129 to solve a large linear system of equations.

130 Here, we review some strategies for reducing the computational cost of equivalent-layer technique. These
 131 strategies are the following:

132 2.2.1 The moving data-window scheme

133 Leão and Silva (1989) reduced the total processing time and memory usage of equivalent-layer technique
 134 by means of a moving data-window scheme. A small moving data window with N_w observations and
 135 a small equivalent layer with M_w equivalent sources ($M_w > N_w$) located below the observations are
 136 established. For each position of a moving-data window, Leão and Silva (1989) estimate a stable solution
 137 \mathbf{p}_w^* by using a data-space approach with the zeroth-order Tikhonov regularization (Aster et al., 2018), i.e.,

$$\left(\mathbf{A}_w \mathbf{A}_w^\top + \mu \mathbf{I} \right) \mathbf{w} = \mathbf{d}_w^o, \quad (3a)$$

$$\mathbf{A}_w^\top \mathbf{w} = \mathbf{p}_w^*, \quad (3b)$$

138 where \mathbf{w} is a dummy vector, μ is a regularizing parameter, \mathbf{d}_w^o is an N_w -dimensional vector containing
 139 the observed potential-field data, \mathbf{A}_w is an $N_w \times M_w$ sensitivity matrix related to a moving-data window, \mathbf{I}
 140 is an identity matrix of order N_w and the superscript \top stands for a transpose. After estimating an $M_w \times 1$
 141 parameter vector \mathbf{p}_w^* (equation 3b) the desired transformation of the data is only calculated at the central
 142 point of each moving-data window, i.e.:

$$\hat{\mathbf{t}}_k = \mathbf{t}_k^\top \mathbf{p}_w^*, \quad (4)$$

143 where $\hat{\mathbf{t}}_k$ is the transformed data calculated at the central point k of the data window and \mathbf{t}_k is an $M_w \times 1$
 144 vector whose elements form the k th row of the $N_w \times N_w$ matrix of Green's functions \mathbf{T} (equation 2) of the
 145 desired linear transformation of the data.

146 By shifting the moving-data window with a shift size of one data spacing, a new position of a data
 147 window is set up. Next, the aforementioned process (equations 3b and 4) is repeated for each position of a
 148 moving-data window, until the entire data have been processed. Hence, instead of solving a large inverse
 149 problem, Leão and Silva (1989) solve several much smaller ones.

150 To reduce the size of the linear system to be solved, Soler and Uieda (2021) adopted the same strategy
 151 proposed, originally, by Leão and Silva (1989) of using a small moving-data window sweeping the whole
 152 data. In Leão and Silva (1989), a moving-data window slides to the next adjacent data window following a
 153 sequential movement, the predicted data is calculated inside the data window and the desired transformation
 154 are only calculated at the center of the moving-data window. Unlike Leão and Silva (1989), Soler and
 155 Uieda (2021) do not adopt a sequential order of the data windows; rather, they adopt a randomized
 156 order of windows in the iterations of the gradient-boosting algorithm (Friedman, 2001 and 2002). The
 157 gradient-boosting algorithm in Soler and Uieda (2021) estimates a stable solution using the data and the
 158 equivalent sources that fall within a moving-data window; however, it calculates the predicted data and the
 159 residual data in the whole survey data. Next, the residual data that fall within a new position of the data
 160 window is used as input data to estimate a new stable solution within the data window which in turn is
 161 used to calculate a new predicted data and a new residual data in the whole survey data. Finally, unlike
 162 Leão and Silva (1989), in Soler and Uieda (2021) neither the data nor the equivalent sources need to be
 163 distributed in regular grids. Indeed, Leão and Silva (1989) built their method using regular grids, but in fact
 164 regular grids are not necessary. Regarding the equivalent-source layout, Soler and Uieda (2021) proposed
 165 the block-averaged sources locations in which the survey area is divided into horizontal blocks and one
 166 single equivalent source is assigned to each block. Each single source per block is placed over the layer
 167 with its horizontal coordinates given by the average horizontal positions of observation points. According
 168 to Soler and Uieda (2021), the block-averaged sources layout reduces the number of equivalent sources
 169 significantly and the gradient-boosting algorithm provides even greater efficiency in terms of data fitting.

170 2.2.2 The equivalent-data concept

171 To reduced the total processing time and memory usage of equivalent-layer technique, Mendonça and
 172 Silva (1994) proposed a strategy called 'equivalent data concept'. The equivalent data concept is grounded
 173 on the principle that there is a subset of redundant data that does not contribute to the final solution and
 174 thus can be dispensed. Conversely, there is a subset of observations, called equivalent data, that contributes
 175 effectively to the final solution and fits the remaining observations (redundant data). Iteractively, Mendonça
 176 and Silva (1994) selected the subset of equivalent data that is substantially smaller than the original dataset.
 177 This selection is carried out by incorporating one data point at a time.

178 According to Mendonça and Silva (1994), the number of equivalent data is about one-tenth of the total
 179 number of observations. These authors used the equivalent data concept to carry out an interpolation of
 180 gravity data. They showed a reduction of the total processing time and memory usage by, at least, two
 181 orders of magnitude as opposed to using all observations in the interpolation process via the classical
 182 equivalent-layer technique.

183 2.2.3 The wavelet compression and lower-dimensional subspace

184 For large data sets, the sensitivity matrix \mathbf{A} (equation 1) is a drawback in applying the equivalent-layer
 185 technique because it is a large and dense matrix.

186 Li and Oldenburg (2010) transformed a large and full sensitivity matrix into a sparse one by using fast
 187 wavelet transforms. In the wavelet domain, Li and Oldenburg (2010) applyied a 2D wavelet transform to
 188 each row and column of the original sensitivity matrix \mathbf{A} to expand it in the wavelet bases. This operation
 189 can be done by premultiplying the original sensitivity matrix \mathbf{A} by a matrix representing the 2D wavelet
 190 transform \mathbf{W}_2 and then the resulting is postmultiplied by the transpose of \mathbf{W}_2 (i.e., \mathbf{W}_2^\top).

$$\tilde{\mathbf{A}} = \mathbf{W}_2 \mathbf{A} \mathbf{W}_2^\top, \quad (5)$$

191 where $\tilde{\mathbf{A}}$ is the expanded original sensitivity matrix in the wavelet bases with many elements zero or close
 192 to zero. Next, the matrix $\tilde{\mathbf{A}}$ is replaced by its sparse version $\tilde{\mathbf{A}}_s$ in the wavelet domain which in turn is
 193 obtained by retaining only the large elements of the $\tilde{\mathbf{A}}$. Thus, the elements of $\tilde{\mathbf{A}}$ whose amplitudes fall
 194 below a relative threshold are discarded. In Li and Oldenburg (2010), the original sensitivity matrix \mathbf{A}
 195 is high compressed resulting in a sparce matrix $\tilde{\mathbf{A}}_s$ with a few percent of nonzero elements and the the
 196 inverse problem is solved in the wavelet domain by using $\tilde{\mathbf{A}}_s$ and a incomplete conjugate gradient least
 197 squares, without an explicit regularization parameter and a limited number of iterations. The solution is
 198 obtained by solving the following linear system

$$\tilde{\mathbf{A}}_L^\top \tilde{\mathbf{A}}_L \tilde{\mathbf{p}}_L^* = \tilde{\mathbf{A}}_L^\top \tilde{\mathbf{d}}^o, \quad (6)$$

199 where $\tilde{\mathbf{p}}_L^*$ is obtained by solving the linear system given by equation 6,

$$\tilde{\mathbf{A}}_L = \tilde{\mathbf{A}}_s \tilde{\mathbf{L}}^{-1}, \quad (7a)$$

$$\tilde{\mathbf{p}}_L = \tilde{\mathbf{L}} \tilde{\mathbf{p}}, \quad (7b)$$

$$\tilde{\mathbf{d}}^o = \mathbf{W}_2 \mathbf{d}^o, \quad (7c)$$

200 where $\tilde{\mathbf{L}}$ is a diagonal and invertible weighting matrix representing the finite-difference approximation in
 201 the wavelet domain. Finally, the distribution over the equivalent layer in the space domain \mathbf{p} is obtained by

202 applying an inverse wavelet transform in two steps, i.e.:

$$\tilde{\mathbf{p}} = \tilde{\mathbf{L}}^{-1} \tilde{\mathbf{p}}_{\mathbf{L}}^*, \quad (8)$$

203 and

$$\mathbf{p} = \mathbf{W}_2 \tilde{\mathbf{p}}. \quad (9)$$

204 Although the data misfit quantifying the difference between the observed and predicted data by the
205 equivalent source is calculated in the wavelet domain, we understand that the desired transformation is
206 calculated via equation 2 which uses a full matrix of Green's functions \mathbf{T} .

207 Li and Oldenburg (2010) used the equivalent-layer technique with a wavelet compression to perform an
208 upward continuation of total-field anomaly between uneven surfaces. For regularly spaced grid of data, Li
209 and Oldenburg (2010) reported that high compression ratios are achieved with insignificant loss of accuracy.
210 As compared to the upward-continued total-field anomaly by equivalent layer using the dense matrix, Li
211 and Oldenburg's (2010) approach, using the Daubechies wavelet, decreased CPU (central processing unit)
212 time by up to two orders of magnitude.

213 Mendonça (2020) overcame the solution of intractable large-scale equivalent-layer problem by using the
214 subspace method (e.g., Skilling and Bryan, 1984; Kennett et al., 1988; Oldenburg et al., 1993; Barbosa
215 et al., 1997). The subspace method reduces the dimension of the linear system of equations to be solved.
216 Given a higher-dimensional space (e.g., M -dimensional model space, \mathbb{R}^M), there exists many lower-
217 dimensional subspaces (e.g., Q -dimensional subspace) of \mathbb{R}^M . The linear inverse problem related to the
218 equivalent-layer technique consists in finding an M -dimension parameter vector $\mathbf{p} \in \mathbb{R}^M$ which adequately
219 fits the potential-field data. The subspace method looks for a parameter vector who lies in a Q -dimensional
220 subspace of \mathbb{R}^M which, in turn, is spanned by a set of Q vectors $\mathbf{v}_i = 1, \dots, Q$, where $\mathbf{v}_i \in \mathbb{R}^M$. In matrix
221 notation, the parameter vector in the subspace method can be written as

$$\mathbf{p} = \mathbf{V} \boldsymbol{\alpha}, \quad (10)$$

222 where \mathbf{V} is an $M \times Q$ matrix whose columns $\mathbf{v}_i = 1, \dots, Q$ form a basis vectors for a subspace Q of \mathbb{R}^M .
223 In equation 10, the parameter vector \mathbf{p} is defined as a linear combination in the space spanned by Q basis
224 vectors $\mathbf{v}_i = 1, \dots, Q$ and $\boldsymbol{\alpha}$ is a Q -dimensional unknown vector to be determined. The main advantage of
225 the subspace method is that the linear system of M equations in M unknowns to be originally solved is
226 reduced to a new linear system of Q equations in Q unknowns which requires much less computational
227 effort since $Q \ll M$, i.e.:

$$\mathbf{V}^\top \mathbf{A}^\top \mathbf{A} \mathbf{V} \boldsymbol{\alpha}^* = \mathbf{V}^\top \mathbf{d}^o. \quad (11)$$

228 To avoid the storage of matrices \mathbf{A} and \mathbf{V} , Mendonça (2020) evaluates an element of the matrix \mathbf{AV} by
229 calculating the dot product between the row of matrix \mathbf{A} and the column of the matrix \mathbf{B} . After estimating
230 $\boldsymbol{\alpha}^*$ (equation 11) belonging to a Q -dimensional subspace of \mathbb{R}^M , the distribution over the equivalent layer
231 \mathbf{p} in the \mathbb{R}^M is obtained by applying equation 10. The choice of the Q basis vectors $\mathbf{v}_i = 1, \dots, Q$ (equation
232 10) in the subspace method is not strict. Mendonça (2020), for example, chose the eigenvectors yielded by
233 applying the singular value decomposition of the matrix containing the gridded data set. The number of
234 eigenvectors used to form basis vectors will depend on the singular values.

235 The proposed subspace method for solving large-scale equivalent-layer problem by Mendonça (2020)
236 was applied to estimate the mass excess or deficiency caused by causative gravity sources.

237 2.2.4 The quadtree discretization

238 To make the equivalent-layer technique tractable, Barnes and Lumley (2011) also transformed the dense
 239 sensitivity matrix \mathbf{A} (equation 1) into a sparse matrix. In Barnes and Lumley (2011), a sparse version of
 240 the sensitivity matrix is achieved by grouping equivalent sources (e.g., they used prisms) distant from an
 241 observation point together to form a larger prism or larger block. Each larger block has averaged physical
 242 properties and averaged top- and bottom-surfaces of the grouped smaller prisms (equivalent sources) that
 243 are encompassed by the larger block. The authors called it the 'larger averaged block' and the essence of
 244 their method is the reduction in the number of equivalent sources, which means a reduction in the number
 245 of parameters to be estimated implying in model dimension reduction.

246 The key of the Barnes and Lumley's (2011) method is the algorithm for deciding how to group the smaller
 247 prisms. In practice, these authors used a recursive bisection process that results in a quadtree discretization
 248 of the equivalent-layer model.

249 By using the quadtree discretization, Barnes and Lumley (2011) were able to jointly process multiple
 250 components of airborne gravity-gradient data using a single layer of equivalent sources. To our knowledge,
 251 Barnes and Lumley (2011) are the pioneers on processing full-tensor gravity-gradient data jointly. In
 252 addition to computational feasibility, Barnes and Lumley's (2011) method reduces low-frequency noise
 253 and can also remove the drift in time-domain from the survey data. Those authors stressed that the
 254 G_{zz} -component calculated through the single estimated equivalent-layer model projected on a grid at a
 255 constant elevation by inverting full gravity-gradient data has the low-frequency error reduced by a factor of
 256 2.4 as compared to the inversion of an individual component of the gravity-gradient data.

257 2.2.5 The reparametrization of the equivalent layer

258 Oliveira Jr. et al. (2013) reparametrized the whole equivalent-layer model by a piecewise bivariate-
 259 polynomial function defined on a set of Q equivalent-source windows. In Oliveira Jr. et al.'s (2013)
 260 approach, named polynomial equivalent layer (PEL), the parameter vector within the k th equivalent-source
 261 window \mathbf{p}^k can be written in matrix notation as

$$\mathbf{p}^k = \mathbf{B}^k \mathbf{c}^k, \quad k = 1 \dots Q, \quad (12)$$

262 where \mathbf{p}^k is an M_w -dimensional vector containing the physical-property distribution within the k th
 263 equivalent-source window, \mathbf{c}^k is a P -dimensional vector whose l th element is the l th coefficient of the
 264 α th-order polynomial function and \mathbf{B}^k is an $M_w \times P$ matrix containing the first-order derivative of the
 265 α th-order polynomial function with respect to one of the P coefficients.

266 By using a regularized potential-field inversion, Oliveira Jr. et al. (2013) estimates the polynomial
 267 coefficients for each equivalent-source window by solving the following linear system

$$(\mathbf{B}^\top \mathbf{A}^\top \mathbf{A} \mathbf{B} + \mu \mathbf{I}) \mathbf{c}^* = \mathbf{B}^\top \mathbf{A}^\top \mathbf{d}^o, \quad (13)$$

268 where μ is a regularizing parameter, \mathbf{c}^* is an estimated H -dimensional vector containing all coefficients
 269 describing all polynomial functions within all equivalent-source windows which compose the entire
 270 equivalent layer, \mathbf{I} is an identity matrix of order H ($H = PQ$) and \mathbf{B} is an $M \times H$ block diagonal matrix
 271 such that the main-diagonal blocks are \mathbf{B}^k matrices (equation 12) and all off-diagonal blocks are zero
 272 matrices. For ease of the explanation of equation 13, we keep only the zeroth-order Tikhonov regularization

273 and omitting the first-order Tikhonov regularization (Aster et al., 2018) which was also used by Oliveira Jr.
274 et al. (2013).

275 The main advantage of the PEL is solve H -dimensional system of equations (equation 13), where H
276 totalizes the number of polynomial coefficients composing all equivalent-source windows, requiring a
277 lower computational effort since $H << N$. To avoid the storage of matrices \mathbf{A} and \mathbf{B} , Oliveira Jr. et al.
278 (2013) evaluate an element of the matrix \mathbf{AB} by calculating the dot product between the row of matrix \mathbf{A}
279 and the column of the matrix \mathbf{B} . After estimating all polynomial coefficients of all windows, the estimated
280 coefficients (\mathbf{c}^* in equation 13) are transformed into a single physical-property distribution encompassing
281 the entire equivalent layer.

282 As stated by Oliveira Jr. et al. (2013), the computational efficiency of PEL approach stems from the fact
283 that the total number of polynomial coefficients H required to depict the physical-property distribution
284 within the equivalent layer is generally much smaller than the number of equivalent sources. Consequently,
285 this leads to a considerably smaller linear system that needs to be solved. Hence, the main strategy of
286 polynomial equivalent layer is the model dimension reduction.

287 The polynomial equivalent layer was applied to perform upward continuations of gravity and magnetic
288 data and reduction to the pole of magnetic data.

289 2.2.6 The iterative scheme without solving a linear system

290 There exists a class of methods that iteratively estimate the distribution of physical properties within an
291 equivalent layer without the need to solve linear systems. The method initially introduced by Cordell (1992)
292 and later expanded upon by Guspi and Novara (2009) updates the physical property of sources, located
293 beneath each potential-field data, by removing the maximum residual between the observed and fitted data.
294 In addition, Xia and Sprowl (1991) and Xia et al. (1993) have developed efficient iterative algorithms for
295 updating the distribution of physical properties within the equivalent layer in the wavenumber and space
296 domains, respectively. Specifically, in Xia and Sprowl's (1991) method the physical-property distribution is
297 updated by using the ratio between the squared depth to the equivalent source and the gravitational constant
298 multiplied by the residual between the observed and predicted observation at the measurement station.
299 Neither of these methods solve linear systems.

300 Following this class of methods of iterative equivalent-layer technique that does not solve linear systems,
301 Siqueira et al. (2017) developed a fast iterative equivalent-layer technique for processing gravity data in
302 which the sensitivity matrix \mathbf{A} (equation 1) is replaced by a diagonal matrix $N \times N$, i.e.:

$$\tilde{\tilde{\mathbf{A}}} = 2\pi\gamma\Delta\mathbf{S}^{-1}, \quad (14)$$

303 where γ is Newton's gravitational constant and $\Delta\mathbf{S}^{-1}$ is a diagonal matrix of order N whose diagonal
304 elements Δs_i , $i = 1, \dots, N$ are the element of area centered at the i th horizontal coordinates of the i th
305 observation point. The physical foundations of Siqueira et al.'s (2017) method rely on two constraints: i) the
306 excess of mass; and ii) the positive correlation between the gravity observations and the mass distribution
307 over the equivalent layer.

308 Although Siqueira et al.'s (2017) method does not solve any linear system of equations, it can be
309 theoretically explained by solving the following linear system at the k th iteration:

$$\tilde{\tilde{\mathbf{A}}}^\top \tilde{\tilde{\mathbf{A}}} \Delta \hat{\mathbf{p}}^k = \tilde{\tilde{\mathbf{A}}}^\top \mathbf{r}^k, \quad (15)$$

310 where \mathbf{r}^k is an N -dimensional residual vector whose i th element is calculated by subtracting the i th
 311 observed data d_i^o from the i th fitted data d_i^k at the k th iteration, i.e.,

$$r_i^k = d_i^o - d_i^k. \quad (16)$$

312 and $\Delta \hat{\mathbf{p}}^k$ is an estimated N -dimensional vector of parameter correction.

313 Because $\tilde{\mathbf{A}}$, in equation 15, is a diagonal matrix (equation 14), the parameter correction estimate is
 314 directly calculated without solving system of linear equations, and thus, an i th element of $\Delta \hat{\mathbf{p}}^k$ is directly
 315 calculated by

$$\Delta \hat{p}_i^k = \frac{\Delta s_i r_i^k}{2 \pi \gamma}. \quad (17)$$

316 The mass distribution over the equivalent layer is updated by:

$$\hat{p}_i^{k+1} = \hat{p}_i^k + \Delta \hat{p}_i^k. \quad (18)$$

317 Siqueira et al.'s (2017) method starts from a mass distribution on the equivalent layer, whose i th mass p_i^o is
 318 proportional to the i th observed data d_i^o , i.e.,

$$p_i^o = \frac{\Delta s_i d_i^o}{2 \pi \gamma}. \quad (19)$$

319 Siqueira et al. (2017) applied their fast iterative equivalent-layer technique to interpolate, calculate the
 320 horizontal components, and continue upward (or downward) gravity data.

321 For jointly process two gravity gradient components, Jirigalatu and Ebbing (2019) used the Gauss-FFT
 322 for forward calculation of potential fields in the wavenumber domain combined with Landweber's iteration
 323 coupled with a mask matrix \mathbf{M} to reduce the edge effects without increasing the computation cost. The
 324 mask matrix \mathbf{M} is defined in the following way: if the corresponding pixel does not contain the original
 325 data, the element of \mathbf{M} is set to zero; otherwise, it is set to one. The k th Landweber iteration is given by

$$\mathbf{p}_{k+1} = \mathbf{p}_k + \omega \left[\mathbf{A}_1^\top (\mathbf{d}_1 - \mathbf{M} \mathbf{A}_1 \mathbf{p}_k) + \mathbf{A}_2^\top (\mathbf{d}_2 - \mathbf{M} \mathbf{A}_2 \mathbf{p}_k) \right], \quad (20)$$

326 where ω is a relaxation factor, \mathbf{d}_1 and \mathbf{d}_2 are the two gravity gradient components and \mathbf{A}_1 and \mathbf{A}_2 are the
 327 corresponding gravity gradient kernels. Jirigalatu and Ebbing (2019) applied their method for processing
 328 two horizontal curvature components of Falcon airborne gravity gradient.

329 2.2.7 The convolutional equivalent layer with BTTB matrices

330 Takahashi et al. (2020, 2022) introduced the convolutional equivalent layer for gravimetric and magnetic
 331 data processing, respectively.

332 Takahashi et al. (2020) demonstrated that the sensitivity matrix \mathbf{A} (equation 1) associated with a planar
 333 equivalent layer formed by a set of point masses, each one directly beneath each observation point and
 334 considering a regular grid of observation points at a constant height has a symmetric block-Toeplitz
 335 block (BTTB) structure. A symmetric BTTB matrix has, at least, two attractive properties. The first one is
 336 that it can be defined by using only the elements forming its first column (or row). The second attractive
 337 property is that any BTTB matrix can be embedded into a symmetric Block-Circulant Circulant-Block

(BCCB) matrix. This means that the full sensitivity matrix \mathbf{A} (equation 1) can be completely reconstruct by using the first column of the BCCB matrix only. In what follows, Takahashi et al. (2020) computed the forward modeling by using only a single equivalent source. Specifically, it is done by calculating the eigenvalues of the BCCB matrix that can be efficiently computed by using only the first column of the BCCB matrix via 2D fast Fourier transform (2D FFT). By comparing with the classic approach in the Fourier domain, the convolutional equivalent layer for gravimetric data processing proposed by Takahashi et al. (2020) performed upward- and downward-continue gravity data with a very small border effects and noise amplification.

By using the original idea of the convolutional equivalent layer proposed by Takahashi et al. (2020) for gravimetric data processing, Takahashi et al. (2022) developed the convolutional equivalent layer for magnetic data processing. By assuming a regularly spaced grid of magnetic data at a constant height and a planar equivalent layer of dipoles, Takahashi et al. (2022) proved that the sensitivity matrix linked with this layer possess a BTTB structure in the specific scenario where each dipole is exactly beneath each observed magnetic data point. Takahashi et al. (2022) used a conjugate gradient least-squares (CGLS) algorithm which does not require an inverse matrix or matrix-matrix multiplication. Rather, it only requires matrix-vector multiplications per iteration, which can be effectively computed using the 2D FFT as a discrete convolution. The matrix-vector product only uses the elements that constitute the first column of the associated BTTB matrix, resulting in computational time and memory savings. Takahashi et al. (2022) showed the robustness of the convolutional equivalent layer in processing magnetic survey that violates the requirement of regular grids in the horizontal directions and flat observation surfaces.

The matrix-vector product in Takahashi et al. (2020, 2022) (e.g., $\mathbf{d} = \mathbf{Ap}$, such as in equation 1) is the main issue to be solved. To solve it efficiently, these authors involved the auxiliary linear system

$$\mathbf{w} = \mathbf{Cv}, \quad (21)$$

where \mathbf{w} and \mathbf{v} are, respectively, vectors of data and parameters completed by zeros and \mathbf{C} is a BCCB matrix formed by $2Q \times 2Q$ blocks, where each block \mathbf{C}_q , $q = 0, \dots, Q - 1$, is a $2P \times 2P$ circulant matrix. The first column of \mathbf{C} is obtained by rearranging the first column of the sensitivity matrix \mathbf{A} (equation 1). Because a BCCB matrix is diagonalized by the 2D unitary discrete Fourier transform (DFT), \mathbf{C} can be written as

$$\mathbf{C} = (\mathbf{F}_{2Q} \otimes \mathbf{F}_{2P})^* \boldsymbol{\Lambda} (\mathbf{F}_{2Q} \otimes \mathbf{F}_{2P}), \quad (22)$$

where the symbol “ \otimes ” denotes the Kronecker product (Neudecker, 1969), \mathbf{F}_{2Q} and \mathbf{F}_{2P} are the $2Q \times 2Q$ and $2P \times 2P$ unitary DFT matrices (Davis, 1979, p. 31), respectively, the superscript “ $*$ ” denotes the complex conjugate and $\boldsymbol{\Lambda}$ is a $4QP \times 4QP$ diagonal matrix containing the eigenvalues of \mathbf{C} . Due to the diagonalization of the matrix \mathbf{C} , the auxiliary system (equation 21) can be rewritten by using equation 22 and premultiplying both sides of the result by $(\mathbf{F}_{2Q} \otimes \mathbf{F}_{2P})$, i.e.,

$$\boldsymbol{\Lambda} (\mathbf{F}_{2Q} \otimes \mathbf{F}_{2P}) \mathbf{v} = (\mathbf{F}_{2Q} \otimes \mathbf{F}_{2P}) \mathbf{w}. \quad (23)$$

By applying the vec-operator (Takahashi et al., 2020) to both sides of equation 23, by premultiplying both sides of the result by \mathbf{F}_{2Q}^* and then postmultiplying both sides of the result by \mathbf{F}_{2P}^*

$$\mathbf{F}_{2Q}^* [\mathbf{L} \circ (\mathbf{F}_{2Q} \mathbf{V} \mathbf{F}_{2P})] \mathbf{F}_{2P}^* = \mathbf{W}, \quad (24)$$

372 where “ \circ ” denotes the Hadamard product (Horn and Johnson, 1991, p. 298) and \mathbf{L} , \mathbf{V} and \mathbf{W} are $2Q \times 2P$
 373 matrices obtained by rearranging, along their rows, the elements forming the diagonal of matrix Λ , vector \mathbf{v}
 374 and vector \mathbf{w} , respectively. The left side of equation 24 contains the 2D Inverse Discrete Fourier Transform
 375 (IDFT) of the term in brackets, which in turn represents the Hadamard product of matrix \mathbf{L} and the 2D
 376 DFT of matrix \mathbf{V} . Matrix \mathbf{L} contains the eigenvalues of Λ (equation 22) and can be efficiently computed
 377 by using only the first column of the BCCB matrix \mathbf{C} (equation 21).

378 Actually, in Takahashi et al. (2020, 2022) a fast 2D discrete circular convolution (Van Loan, 1992) is
 379 used to process very large gravity and magnetic datasets efficiently. The convolutional equivalent layer
 380 was applied to perform upward continuation of large magnetic datasets. Compared to the classical Fourier
 381 approach, Takahashi et al.’s (2022) method produces smaller border effects without using any padding
 382 scheme.

383 Without taking advantage of the symmetric BTTB structure of the sensitivity matrix (Takahashi et al.,
 384 2020) that arises when gravimetric observations are measured on a horizontally regular grid, on a flat
 385 surface and considering a regular grid of equivalent sources whithin a horizontal layer, Mendonça (2020)
 386 explored the symmetry of the gravity kernel to reduce the number of forward model evaluations. By
 387 exploting the symmetries of the gravity kernels and redundancies in the forward model evaluations on a
 388 regular grid and combining the subspace solution based on eigenvectors of the gridded dataset, Mendonça
 389 (2020) estimated the mass excess or deficiency produced by anomalous sources with positive or negative
 390 density contrast.

391 2.2.8 The deconvolutional equivalent layer with BTTB matrices

392 To avoid the iterations of the conjugate gradient method in Takahashi et al. (2022), we can employ the
 393 deconvolution process. Equation 24 shows that estimate the matrix \mathbf{V} , containing the elements of parameter
 394 vector \mathbf{p} , is a inverse problem that could be solved by deconvolution. From equation 24, the matrix \mathbf{V} can
 395 be obtain by deconvolution, i.e.

$$\mathbf{V} = \mathbf{F}_{2Q}^* \left[\frac{(\mathbf{F}_{2Q} \mathbf{W} \mathbf{F}_{2P})}{\mathbf{L}} \right] \mathbf{F}_{2P}^*. \quad (25)$$

396 Equation 25 shows that the parameter vector (in matrix \mathbf{V}) can be theoretically obtain by dividing each
 397 potential-field observations (in matrix \mathbf{W}) by each eigenvalues (in matrix \mathbf{L}). Hence, the parameter vector
 398 is constructed by element-by-element division of data by eigenvalues.

399 However, the deconvolution often is extremely unstable. This means that a small change in data can lead
 400 to an enormous change in the estimated parameter. Hence, equation 25 requires regularization to be useful.
 401 We usede wiener deconvolution to obtain a stable solution, i.e.,

$$\mathbf{V} = \mathbf{F}_{2Q}^* \left[(\mathbf{F}_{2Q} \mathbf{W} \mathbf{F}_{2P}) \frac{\mathbf{L}^*}{(\mathbf{L} \mathbf{L}^* + \mu)} \right] \mathbf{F}_{2P}^*, \quad (26)$$

402 where the matrix \mathbf{L}^* contains the complex conjugate eigenvalues and μ is a parameter that controls the
 403 degree of stabilization.

404 2.3 Solution stability

405 The solution stability of the equivalent-layer methods is rarely addressed. Here, we follow the numerical
 406 stability analysis presented in Siqueira et al. (2017).

407 Let us assume noise-free potential-field data \mathbf{d} , we estimate a physical-property distribution \mathbf{p} (estimated
 408 solution) within the equivalent layer. Then, the noise-free data \mathbf{d} are contaminated with additive D different
 409 sequences of pseudorandom Gaussian noise, creating different noise-corrupted potential-field data \mathbf{d}_ℓ^o ,
 410 $\ell = 1, \dots, D$. From each \mathbf{d}_ℓ^o , we estimate a physical-property distribution $\hat{\mathbf{p}}_\ell$ within the equivalent layer.

411 Next, for each noise-corrupted data \mathbf{d}_ℓ^o and estimated solution $\hat{\mathbf{p}}_\ell$, the ℓ th model perturbation δp_ℓ and the
 412 ℓ th data perturbation δd_ℓ are, respectively, evaluated by

$$\delta p_\ell = \frac{\|\hat{\mathbf{p}}_\ell - \mathbf{p}\|_2}{\|\mathbf{p}\|_2}, \quad \ell = 1, \dots, D, \quad (27)$$

413 and

$$\delta d_\ell = \frac{\|\mathbf{d}_\ell^o - \mathbf{d}\|_2}{\|\mathbf{d}\|_2}, \quad \ell = 1, \dots, D. \quad (28)$$

414 Regardless of the particular method used, the following inequality (Aster et al., 2018, p. 66) is applicable:

$$\delta p_\ell \leq \kappa \delta d_\ell, \quad \ell = 1, \dots, D, \quad (29)$$

415 where κ is the constant of proportionality between the model perturbation δp_ℓ (equation 27) and the data
 416 perturbation δd_ℓ (equation 28). The constant κ acts as the condition number of an invertible matrix in a
 417 given inversion, and thus measures the instability of the solution. The larger (smaller) the value of κ the
 418 more unstable (stable) is the estimated solution.

419 Equation 29 shows a linear relationship between the model perturbation and the data perturbation. By
 420 plotting δp_ℓ (equation 27) against δd_ℓ (equation 28) produced by a set of D estimated solution obtained by
 421 applying a given equivalent-layer method, we obtain a straight line behaviour described by equation 29.
 422 By applying a linear regression, we obtain a fitted straight line whose estimated slope (κ in equation 29)
 423 quantifies the solution stability.

424 Here, the analysis of solution stability is numerically conducted by applying the classical equivalent-
 425 layer technique with zeroth-order Tikhonov regularization, the convolutional method for gravimetric and
 426 magnetic data, the deconvolutional method (equation 25) and the deconvolutional method with different
 427 values for the Wiener stabilization (equation 26).

3 NUMERICAL SIMULATIONS

428 3.1 Floating-point operations calculation

429 To measure the computational effort of the different algorithms to solve the equivalent layer linear system,
 430 a non-hardware dependent method can be useful because allow us to do direct comparison between them.
 431 Counting the floating-point operations (*flops*), i.e., additions, subtractions, multiplications and divisions is
 432 a good way to quantify the amount of work of a given algorithm (Golub and Loan, 2013). For example, the
 433 number of *flops* necessary to multiply two vectors \mathbb{R}^N is $2N$. A common matrix-vector multiplication with
 434 dimension $\mathbb{R}^{N \times N}$ and \mathbb{R}^N , respectively, is $2N^2$ and a multiplication of two matrices $\mathbb{R}^{N \times N}$ is $2N^3$. Figure
 435 1 shows the total flops count for the different methods presented in this review with a crescent number of
 436 data, ranging from 10,000 to 1,000,000 for the gravity equivalent layer and figure 2 for magnetic data.

437 3.1.1 Normal equations using Cholesky decomposition

438 The equivalent sources can be estimated directly from solving the normal equations 2. In this work we
 439 will use the Cholesky decompositions method to calculate the necessary *flops*. In this method it is calculated
 440 the lower triangule of $\mathbf{A}^T \mathbf{A}$ ($1/2N^3$), the Cholesky factor ($1/3N^3$), a matrix-vector multiplication ($2N^2$)
 441 and finally solving the triangular system ($2N^2$), totalizing

$$f_{classical} = \frac{5}{6}N^3 + 4N^2 \quad (30)$$

442 3.1.2 Window method (Leão and Silva, 1989)

443 The moving data-window scheme (Leão and Silva, 1989) solve N linear systems with much smaller
 444 sizes (equation 3b) in comparison to the original $N \times N$ system. For our results we are considering a
 445 data-window of the same size of which the authors presented in theirs work ($N_w = 49$) and the same number
 446 of equivalent sources ($M_w = 225$). Using the Cholesky decomposition with this method the *flops* are

$$f_{window} = N \frac{5}{6} M_w N_w^2 + 4N_w M_w \quad (31)$$

447 3.1.3 PEL method (Oliveira Jr. et al., 2013)

448 The polynomial equivalent layer uses a similiar approach of moving windows from Leão and Silva (1989).
 449 For this operations calculation (equation 13) we used a first degree polynomial (two variables) and each
 450 window contains $N_s = 1,000$ observed data and $M_s = 1,000$ equivalent sources. Following the steps
 451 given in (Oliveira Jr. et al., 2013) the total *flops* becomes

$$f_{pel} = \frac{1}{3}H^3 + 2H^2 + 2NM_sH + H^2N + 2HN + 2NP \quad (32)$$

452 where H is the number of constant coefficients for the first degree polynomial ($P = 3$) times the number
 453 of windows ($P \times N/N_s$).

454 3.1.4 Conjugate gradient least square (CGLS)

455 The CGLS method is a very stable and fast algorithm for solving linear systems iteratively. Its computa-
 456 tional complexity envolves a matrix-vector product outside the loop ($2N^2$), two matrix-vector products
 457 inside the loop ($4N^2$) and six vector products inside the loop ($12N$) (Aster et al., 2018)

$$f_{ccls} = 2N^2 + it(4N^2 + 12N) \quad (33)$$

458 3.1.5 Wavelet compression method with CGLS (Li and Oldenburg, 2010)

459 For the wavelet method (equation 6) we have calculated a compression rate of 98% ($C_r = 0.02$) as
 460 the authors used in Li and Oldenburg (2010) and the wavelet transformation requiring $\log_2(N)$ flops each
 461 (equations 5 and 7c), with its inverse also using the same number of operations (equation 9). Combined
 462 with the conjugate gradient least square necessary steps and iterations, the number of flops are

$$f_{wavelet} = 2NC_r + 4N \log_2(N) + it(4N \log_2(N) + 4NC_r + 12C_r) \quad (34)$$

463 3.1.6 Fast equivalent layer for gravity data (Siqueira et al., 2017)

464 The fast equivalent layer from Siqueira et al. (2017) solves the linear system in it iterations. The main
 465 cost of this method (equations 15, 16, 17 and 18) is the matrix-vector multiplication to asses the predicted
 466 data ($2N^2$) and three simply element by element vector sum, subtraction and division (3N total)

$$f_{siqueira} = it(3N + 2N^2) \quad (35)$$

467 3.1.7 Convolutional equivalent layer for gravity data (Takahashi et al., 2020)

468 This methods replaces the matrix-vector multiplication of the iterative fast-equivalent technique (Siqueira
 469 et al., 2017) by three steps, involving a Fourier transform, an inverse Fourier transform, and a Hadamard
 470 product of matrices (equation 24). Considering that the first column of our BCCB matrix has $4N$ elements,
 471 the flops count of this method is

$$f_{convgrav} = \kappa 4N \log_2(4N) + it(27N + \kappa 8N \log_2(4N)) \quad (36)$$

472 In the resultant count we considered a *radix-2* algorithm for the fast Fourier transform and its inverse,
 473 which has a κ equals to 5 and requires $\kappa 4N \log_2(4N)$ flops each. The Hadarmard product of two matrices
 474 of $4N$ elements with complex numbers takes $24N$ flops. Note that equation 36 is different from the one
 475 presented in Takahashi et al. (2020) because we also added the flops necessary to calculate the eigenvalues
 476 in this form. It does not differentiate much in order of magnitude because the iterative part is the most
 477 costful.

478 3.1.8 Convolutional equivalent layer for magnetic data (Takahashi et al., 2022)

479 The convolutional equivalent layer for magnetic data uses the same flops count of the main operations as
 480 in the gravimetric case (equation 24), the difference is the use of the conjugate gradient algorithm to solve
 481 the inverse problem. It requires a Hadamard product outside of the iterative loop and the matrix-vector and
 482 vector-vector multiplications inside the loop as seem in equation 33.

$$f_{convmag} = \kappa 16N \log_2(4N) + 24N + it(\kappa 16N \log_2(4N) + 60N) \quad (37)$$

483 3.1.9 Deconvolutional method

484 The deconvolution method does not require an iterative algorithm, rather it solves the estimative of the
485 physical properties in a single step using the $4N$ eigenvalues of the BCCB matrix as in the convolutional
486 method. From equation 25 it is possible to deduce this method requires two fast Fourier transform
487 ($\kappa 4N \log_2(4N)$), one for the eigenvalues and another for the data transformation, an element by element
488 division ($24N$) and finally, a fast inverse Fourier transform for the final estimative ($\kappa 4N \log_2(4N)$).

$$f_{deconv} = \kappa 12N \log_2(4N) + 24N \quad (38)$$

489 Using the deconvolutional method with a Wiener stabilization adds two multiplications of complex
490 elements of the conjugates eigenvalues ($24N$ each) and the sum of $4N$ elements with the stabilization
491 parameter μ as shown in equation 26

$$f_{deconvwiener} = \kappa 12N \log_2(4N) + 76N \quad (39)$$

4 SYNTHETIC DATA SIMULATIONS

492 For all applications, we generate a model composed by two spheres and a polygonal prism in a regular
 493 spaced grid of 50×50 . The upper left sphere has a density contrast of 600 kg/m^3 , the right upper sphere a
 494 negative contrast of -500 kg/m^3 and the bottom prism is equal to 550 kg/m^3 . To generate the magnetic
 495 data, the bodies are in the same position and all of them have the same magnetization intensity and
 496 direction (3.46 A/m intensity, 35.26° inclination and 45.0° declination) within a simulated geomagnetic
 497 field direction of 20.0° inclination and 35.0° declination. These synthetic datas are shown in figures 4 and
 498 8, respectively.

499 4.1 Stability analysis

500 For the stability analysis we show the comparison of the normal equations solution (equation 2) with
 501 zeroth-order Tikhonov regularization (Aster et al., 2018), the convolutional method (equation 24), the
 502 deconvolutional method (equation 25) and the deconvolutional method with different values for the Wiener
 503 stabilization (equation 26). We create 21 data sets, for both gravity and magnetic data, adding a crescent
 504 pseudo-random noise to the original data, which varies from 0% to 10% of the maximum anomaly value in
 505 intervals of 0.5%. These noises has mean equal to zero and a Gaussian distribution. These synthetic datas
 506 are shown in figures 4 and 8, where panel (A) of each figure represents the noise free data and panel (B) is
 507 the maximum noised data for gravity and magnetic, respectively.

508 Figure 3 shows how the euclidian norm of the equivalent sources residuals varies as the level of the noise
 509 is increased for the gravimetric data. We can see that for all methods, a linear tendency can be observed as
 510 it is expected. The inclination of the straight line is a indicative of the stability of each method. As show
 511 in the graph the deconvolutional method is very unstable and it is really necessary to use a stabilization
 512 method to have a good parameter estimative. In contrast, a correct value of the stabilization parameter is
 513 necessary to not overshoot the smoothness of the solution as it is the case for the zeroth-order Tikhonov
 514 regularization as well. Using this gravimetric data, the optimal value for the Wiener stabilization parameter
 515 is $\mu = 10^{-20}$.

516 Figure 5 shows the comparison of the predicted data for each method with the original data (figure 4)
 517 using the most noised-corrupted data from the set of the stability analysis. The classical with zeroth-order
 518 Tikhonov regularization and the convolutional methods (figures 5(A) and 5(B)) yield very similar results for
 519 the predicted data confirming its similarities with the stabilization despite the bid difference in floating-point
 520 operations. Figure 5(C) shows the deconvolutional method without a stabilization and demonstrates the
 521 necessity to use it for this method. Figure 5(D) shows the deconvolutional method with Wiener stabilization
 522 $\mu = 10^{-15}$ which is too high, demonstrating the over smoothness of the predicted data. Figures 5(E) and
 523 5(F) shows the predicted data for an optimal value of the Wiener parameter $\mu = 10^{-20}$ and a low value
 524 $\mu = 10^{-25}$, respectively.

525 The upward continuation is a processing technique to visualize the data in a higher altitude. In practice is
 526 expected a lower amplitude signal and a smoother data as the high frequency anomalies tends to disappear.
 527 Figure 6(A) shows the true modeled upward data at an height of -500 m . Figures 6(B), (C), (D) and
 528 (E) show the result of the upward processing for the classical, convolutional, deconvolutional and the
 529 deconvolutional with Wiener parameter $\mu = 10^{-20}$, respectively. It is clear that all methods seems to
 530 predict the upward data very reasonable, except the deconvolutional method without stabilization.

531 For the magnetic data, figure 7 shows a very similar behavior of the stability as the previous case. The
 532 Wiener parameter seems to have the best solution for $\mu = 10^{-13}$. For both types of data the best Wiener

533 parameter seems to be one that produces a low slope for the straight line in the stability analysis, discordant
534 from the classical and convolutional methods.

535 Figure 9 shows the comparison of the predicted data for each method with the original magnetic data in
536 figure 8 using the most noised-corrupted data modeled from the stability analysis. As the previous case the
537 classical (figure 9(A)) and the convolutional (figure 9(B)) methods have very similar predicted data but
538 estimated with less orders of magnitude in floating-point operations. The deconvolutional (figure 9(C)) have
539 have a strong disagreement with the observed data showing the need for a stabilization method. Figure
540 9(D) has a value of $\mu = 10^{-10}$ and the predicted data became to smooth by it. The optimal value of the
541 Wiener parameter is shown in figure 9(E) with $\mu = 10^{-13}$ and figure 9(F) shows a predicted data with a
542 low stabilization value with $\mu = 10^{-16}$.

543 Figure 10(A) shows the true modeled upward data at an height of -1400 m. Figures 10(B), (C), (D)
544 and (E) show the result of the upward processing for the classical, convolutional, deconvolutional and the
545 deconvolutional with Wiener parameter $\mu = 10^{-13}$, respectively. As in the gravimetric case, all methods
546 seems to predict the upward data, except the deconvolutional method without stabilization.

5 REAL DATA RESULTS

547 In this section, we show the applications of the convolutional and the deconvolutional strategies in a real
548 data set from the North of Brazil. The region is located in the Carajás Mineral Province (CMP) in the
549 Amazon craton (Moroni et al., 2001; Villas and Santos, 2001). This area is known for its intensive mineral
550 exploration such as iron, copper, gold, manganese, and, recently, bauxite.

551 5.1 Geological setting

552 The Amazon craton is one of the largest and least-known Archean-Proterozoic areas in the world,
553 comprehending a region with a thousand square kilometers. It is one of the main tectonic units in South
554 America, which is covered by five Phanerozoic basins: Maranhão (Northeast), Amazon (Central), Xingu-
555 Alto Tapajós (South), Parecis (Southwest), and Solimões (West). The craton is limited by the Andean
556 Orogenic Belt to the west and the by Araguaia Fold Belt to the east and southeast. The Amazon craton has
557 been subdivided into provinces according to two models, one geochronological and the other geophysical-
558 structural (Amaral, 1974; Teixeira et al., 1989; Tassinari and Macambira, 1999). Thus, seven geological
559 provinces with distinctive ages, evolution, and structural patterns can be observed, namely : (i) Carajás with
560 two domains - the Mesoarchean Rio Maria and Neoarchean Carajás; (ii) Archean-Paleoproterozoic Central
561 Amazon, with Iriri-Xingu and Curuá-Mapuera domains; (ii) Trans-Amazonian (Ryacian), with the Amapá
562 and Bacajá domains; (iv) the Orosinian Tapajós-Parima, with Peixoto de Azevedo, Tapajós, Uaimiri, and
563 Parima domains; (v) Rondônia-Juruena (Statherian), with Jamari, Juruena, and Jauru domains; (vi) The
564 Statherian Rio Negro, with Rio Negro and Imeri domains; and (vii) Sunsás (Meso-Neoproterozoic), with
565 Santa Helena and Nova Brasilândia domains (Santos et al., 2000). Nevertheless, we focus this work only
566 on the Carajás Province.

567 The Carajás Mineral Province (CMP) is located in the east-southeast region of the craton, within an old
568 tectonically stable nucleus in the South American Plate that became tectonically stable at the beginning of
569 Neoproterozoic (Salomao et al., 2019). This area has been the target of intensive exploration at least since
570 the final of the '60s, after the discovery of large iron ore deposits. There are several greenstone belts in the
571 region, among them are the Andorinhas, Inajá, Cumaru, Carajás, Serra Leste, Serra Pelada, and Sapucaia
572 (Santos et al., 2000). The mineralogic and petrologic studies in granite stocks show a variety of minerals
573 found in the province, such as amphibole, plagioclase, biotite, ilmenite, and magnetite (Cunha et al., 2016).
574 These two latter minerals contribute to the high magnetic response in the CMP area. This fact opens the
575 opportunity for potential field applications for the geophysical description of the area.

576 5.2 Potential field data applications

577 Here we compare the performance of the convolutional and deconvolutional algorithms in a real potential
578 field data set. We focus the application on a region in the Southeast of the State of Pará. The aeromagnetic
579 data were acquired by the Geological Survey of Brazil-CPRM. The survey area covers $\approx 58000 \text{ km}^2$ with
580 high-resolution gravity and magnetic data. The flight and the tie lines were acquired and spaced at 3 km
581 and 12 km oriented in the directions $N - S$ and $E - W$, respectively, with a mean flight height of 900 m
582 above the ground. For both applications, we interpolated gravity and magnetic anomalies data, calculating
583 the data set in a grid of 1000×500 ($N = 500000$ observation points) at the same mean flight height. About
584 the computational resources, we processed both data on an Intel Core i7 7700HQ@2.8 GHz processor and
585 16GB RAM. We show in Figure 11 and Figure 13 the interpolated aerogravimetric and aeromagnetic data,
586 respectively. We also use the same equivalent layer grid configuration in gravity and magnetic applications.

587 This setup is composed by a grid of 1000×500 equivalent sources (a total number of $M = 500000$ points)
588 positioned below the observation plane, but a different depth in each application.

589 We apply both strategies to the gravimetric case. We set a depth for the equivalent layer equal to 1200 m
590 below the observation plane. Figure 12A and Figure 12C show the predicted data for convolutional and
591 deconvolutional strategies. The residual maps (the difference between the observed and predicted data)
592 are show in figures 12B and 12D for the convolutional and deconvolutional equivalent-layer technique,
593 respectively. For the convolutional case, the mean residual and standard deviation values are $\approx 0.00\text{ mGal}$
594 and $\approx 0.15\text{ mGal}$, respectively. For the deconvolutional case, the mean residual and standard deviation
595 values are $\approx 0.46\text{ mGal}$ and $\approx 1.23\text{ mGal}$, respectively. These last results show that the estimated density
596 distributions (not shown) fit the observed data for both applications. To show the performance of the
597 algorithms, we performed an upward continuation by using the estimated density distributions (figures 12E
598 and 12F). There is a little difference on the processing time between both strategies. The convolutional
599 algorithm took $\approx 9.18\text{s}$ and the deconvolutional algorithm took $\approx 0.53\text{s}$. We conclude that both strategies
600 are capable of processing gravimetric observations from large areas with dense coverage data. Despite a
601 little difference in processing time, the deconvolutional equivalent-layer technique proved to be faster than
602 the convolutional strategy.

603 Finally, we test the convolutional and deconvolutional algorithms for processing total-field anomalies.
604 We stress that the Carajás area is very large and the main field direction varies significantly. For this reason,
605 we consider a mean direction for the main field equal to -19.865° and -7.43915° (the same as the mid
606 location of the area) for the inclination and declination, respectively. Furthermore, we are not considering
607 the knowledge about the magnetization direction of the sources, and choose a magnetization direction for
608 the equivalent layer equal to the main field direction. For this application, we set a depth of 900 m (below
609 the observation plane) for the equivalent layer. Figure 13A and Figure 13C show the predicted data for
610 convolutional and deconvolutional algorithms. The residual maps (the difference between the observed and
611 predicted data) are show in figures 13B and 13D for the convolutional and deconvolutional techniques,
612 respectively. The convolutional equivalent layer produced a mean residual and standard deviation values
613 of $\approx 0.06\text{ nT}$ and $\approx 1.97\text{ nT}$, respectively. The deconvolutional algorithm produced a mean residual
614 and standard deviation values of $\approx 18.99\text{ nT}$ and $\approx 33.64\text{ nT}$, respectively. To show the performance
615 of the algorithms, we performed an upward continuation (figures 13E and 13F) by using the estimated
616 magnetic-moment distributions (not shown). Similarly to the gravity application, the deconvolutional
617 equivalent layer presents faster results than the convolutional algorithm. The deconvolutional and the
618 convolutional approaches took $\approx 0.89\text{s}$ and $\approx 82.08\text{s}$, respectively. Despite the difference between the
619 processing time of both strategies and considering the mean value of residuals and standard deviations, we
620 conclude that the convolutional strategy fits the observation data better than the deconvolutional approach.

6 DISCUSSION AND CONCLUSION

CONFLICT OF INTEREST STATEMENT

621 The authors declare that the research was conducted in the absence of any commercial or financial
622 relationships that could be construed as a potential conflict of interest.

AUTHOR CONTRIBUTIONS

623 The Author Contributions section is mandatory for all articles, including articles by sole authors. If an
624 appropriate statement is not provided on submission, a standard one will be inserted during the production
625 process. The Author Contributions statement must describe the contributions of individual authors referred
626 to by their initials and, in doing so, all authors agree to be accountable for the content of the work. Please
627 see here for full authorship criteria.

FUNDING

628 Diego Takahashi was supported by a Post-doctoral scholarship from CNPq (grant 300809/2022-0) Valéria
629 C.F. Barbosa was supported by fellowships from CNPq (grant 309624/2021-5) and FAPERJ (grant
630 26/202.582/2019). Vanderlei C. Oliveira Jr. was supported by fellowships from CNPq (grant 315768/2020-
631 7) and FAPERJ (grant E-26/202.729/2018).

ACKNOWLEDGMENTS

632 We thank the Brazilian federal agencies CAPES, CNPq, state agency FAPERJ and Observatório Nacional
633 research institute and Universidade do Estado do Rio de Janeiro.

DATA AVAILABILITY STATEMENT

634 The datasets generated for this study can be found in the frontiers-paper Github repository link:
635 <https://github.com/DiegoTaka/frontiers-paper>.

REFERENCES

- 636 Amaral, G. (1974). *Geologia Pré-Cambriana da Região Amazônica*. Ph.D. thesis, Universidade de São
637 Paulo
- 638 Aster, R. C., Borchers, B., and Thurber, C. H. (2018). *Parameter estimation and inverse problems*
639 (Elsevier)
- 640 Barbosa, V. C. F., Silva, J. B., and Medeiros, W. E. (1997). Gravity inversion of basement relief using
641 approximate equality constraints on depths. *Geophysics* 62, 1745–1757
- 642 Barnes, G. and Lumley, J. (2011). Processing gravity gradient data. *Geophysics* 76, I33–I47. doi:10.1190/
643 1.3548548
- 644 Cordell, L. (1992). A scattered equivalent-source method for interpolation and gridding of potential-field
645 data in three dimensions. *Geophysics* 57, 629–636
- 646 Cunha, I. R., Dall’Agnol, R., and Feio, G. R. L. (2016). Mineral chemistry and magnetic petrology of the
647 archean planalto suite, carajás province – amazonian craton: Implications for the evolution of ferroan
648 archean granites. *Journal of South American Earth Sciences* 67, 100–121
- 649 Dampney, C. N. G. (1969). The equivalent source technique. *Geophysics* 34, 39–53. doi:10.1190/1.
650 1439996

- 651 Davis, K. and Li, Y. (2011). Fast solution of geophysical inversion using adaptive mesh, space-filling
652 curves and wavelet compression. *Geophysical Journal International* 185, 157–166. doi:10.1111/j.
653 1365-246X.2011.04929.x
- 654 Davis, P. J. (1979). *Circulant matrices* (John Wiley & Sons, Inc.)
- 655 Friedman, J. H. (2001). Greedy function approximation: a gradient boosting machine. *Annals of statistics* ,
656 1189–1232
- 657 Friedman, J. H. (2002). Stochastic gradient boosting. *Computational statistics and data analysis* 38,
658 367–378
- 659 Golub, G. H. and Loan, C. F. V. (2013). *Matrix Computations (Johns Hopkins Studies in the Mathematical
660 Sciences)* (Johns Hopkins University Press), 4 edn.
- 661 Guspí, F. and Novara, I. (2009). Reduction to the pole and transformations of scattered magnetic data using
662 newtonian equivalent sources. *Geophysics* 74, L67–L73
- 663 Horn, R. A. and Johnson, C. R. (1991). *Topics in Matrix Analysis* (Cambridge University Press), 1 edn.
- 664 Jirigalatu, J. and Ebbing (2019). A fast equivalent source method for airborne gravity gradient data.
665 *Geophysics* 84, G75–G82. doi:10.1190/GEO2018-0366.1
- 666 Kellogg, O. D. (1929). *Foundations of Potential Theory* (Frederick Ungar Publishing Company)
- 667 Kennett, B., Sambridge, M., and Williamson, P. (1988). Subspace methods for large inverse problems with
668 multiple parameter classes. *Geophysical Journal International* 94, 237–247
- 669 Leão, J. W. D. and Silva, J. B. C. (1989). Discrete linear transformations of potential field data. *Geophysics*
670 54, 497–507. doi:10.1190/1.1442676
- 671 Li, Y. and Oldenburg, D. W. (2010). Rapid construction of equivalent sources using wavelets. *Geophysics*
672 75, L51–L59. doi:10.1190/1.3378764
- 673 Mendonça, C. A. (2020). Subspace method for solving large-scale equivalent layer and density mapping
674 problems. *Geophysics* 85, G57–G68. doi:10.1190/geo2019-0302.1
- 675 Mendonça, C. A. and Silva, J. B. C. (1994). The equivalent data concept applied to the interpolation of
676 potential field data. *Geophysics* 59, 722–732. doi:10.1190/1.1443630
- 677 Moroni, M., Girardi, V., and Ferrario, A. (2001). The serra pelada au-pge deposit, serra dos carajás (pará
678 state, brazil): geological and geochemical indications for a composite mineralising process. *Mineralium
679 Deposita* 36, 768–785
- 680 Neudecker, H. (1969). Some theorems on matrix differentiation with special reference to kronecker matrix
681 products. *Journal of the American Statistical Association* 64, 953–963. doi:10.1080/01621459.1969.
682 10501027
- 683 Oldenburg, D., McGillivray, P., and Ellis, R. (1993). Generalized subspace methods for large-scale inverse
684 problems. *Geophysical Journal International* 114, 12–20
- 685 Oliveira Jr., V. C., Barbosa, V. C. F., and Uieda, L. (2013). Polynomial equivalent layer. *Geophysics* 78,
686 G1–G13. doi:10.1190/geo2012-0196.1
- 687 Salomao, G. N., Dall’Agnol, R., Angelica, R. S., Figueiredo, M. A., Sahoo, P. K., Medeiros-filho, C. A.,
688 et al. (2019). Geochemical mapping and estimation of background concentrations in soils of carajás
689 mineral province, eastern amazonian craton, brazil. *Geochemistry: Exploration, Environment, Analysis*
690 19, 431–447
- 691 Santos, J. O. S., Hartmann, L. A., Gaudette, H. E., Groves, D. I., Mcnaughton, M. J., and Fletcher, I. R.
692 (2000). A new understanding of the provinces of the amazon craton based on integration of field mapping
693 and u-pb and sm-nd geochronology. *Gondwana Research* 3, 453–488
- 694 Siqueira, F. C., Oliveira Jr, V. C., and Barbosa, V. C. (2017). Fast iterative equivalent-layer technique for
695 gravity data processing: A method grounded on excess mass constraint. *Geophysics* 82, G57–G69

- 696 Skilling, J. and Bryan, R. (1984). Maximum entropy image reconstruction-general algorithm. *Monthly*
697 *Notices of the Royal Astronomical Society, Vol. 211, NO. 1, P. 111, 1984* 211, 111
- 698 Soler, S. R. and Uieda, L. (2021). Gradient-boosted equivalent sources. *Geophysical Journal International*
699 227, 1768–1783. doi:10.1093/gji/ggab297
- 700 Takahashi, D., Oliveira, V. C., and Barbosa, V. C. (2022). Convolutional equivalent layer for magnetic data
701 processing. *Geophysics* 87, 1–59
- 702 Takahashi, D., Oliveira Jr, V. C., and Barbosa, V. C. (2020). Convolutional equivalent layer for gravity data
703 processing. *Geophysics* 85, G129–G141
- 704 Tassinari, C. C. and Macambira, M. J. (1999). Geochronological provinces of the amazonian craton.
705 *Episodes* 22, 174–182
- 706 Teixeira, W., Tassinari, C., Cordani, U. G., and Kawashita, K. (1989). A review of the geochronology of
707 the amazonian craton: Tectonic implications. *Precambrian Research* 42, 213–227
- 708 Van Loan, C. (1992). *Computational Frameworks for the Fast Fourier Transform* (SIAM)
- 709 Villas, R. N. and Santos, M. (2001). Gold deposits of the carajás mineral province: deposit types and
710 metallogenesis. *Mineralium Deposita* 36, 300–331
- 711 Xia, J. and Sprowl, D. R. (1991). Correction of topographic distortion in gravity data. *Geophysics* 56,
712 537–541
- 713 Xia, J., Sprowl, D. R., and Adkins-Heljeson, D. (1993). Correction of topographic distortions in potential-
714 field data; a fast and accurate approach. *Geophysics* 58, 515–523. doi:10.1190/1.1443434

7 SUPPLEMENTARY TABLES AND FIGURES

715 7.1 Figures

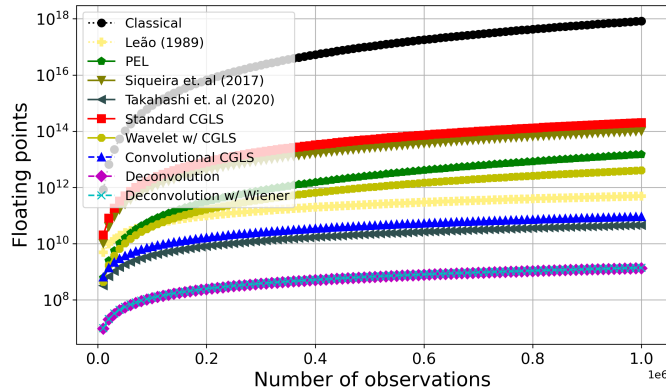


Figure 1. Number of *flops* for many of the methods described in this work to estimate the equivalent sources using gravity data. The range of observations varies from 10,000 to 1,000,000.

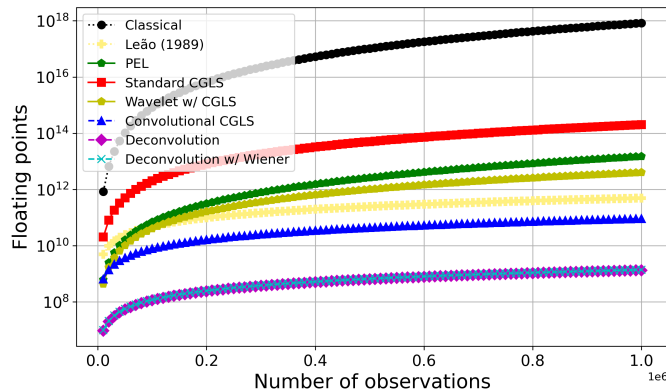


Figure 2. Number of *flops* for many of the methods described in this work to estimate the equivalent sources using magnetic data. The range of observations varies from 10,000 to 1,000,000.

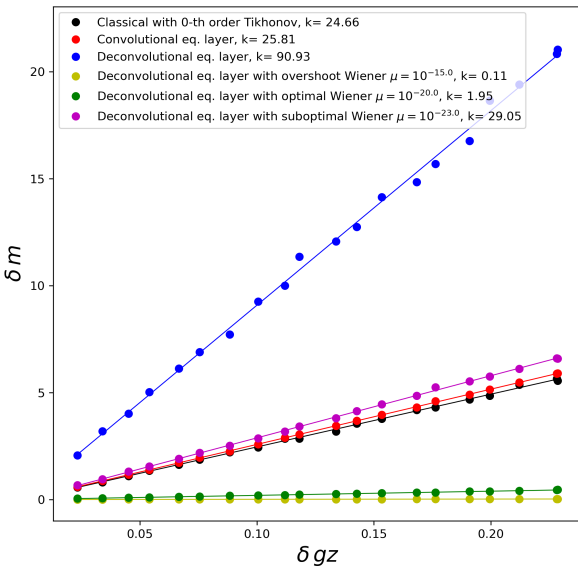


Figure 3. Stability analysis of some of the equivalent layer methods of the gravimetric case.

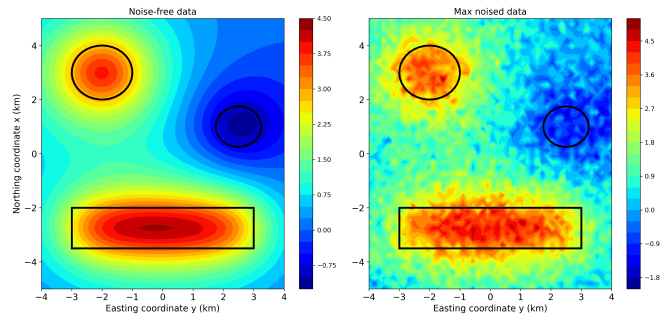


Figure 4. Synthetic data of the gravimetric case. The observations points are placed in a regular grid of 50×50 . Panel (A) shows the noise-free data and panel (B) shows the maximum noised data (10%).

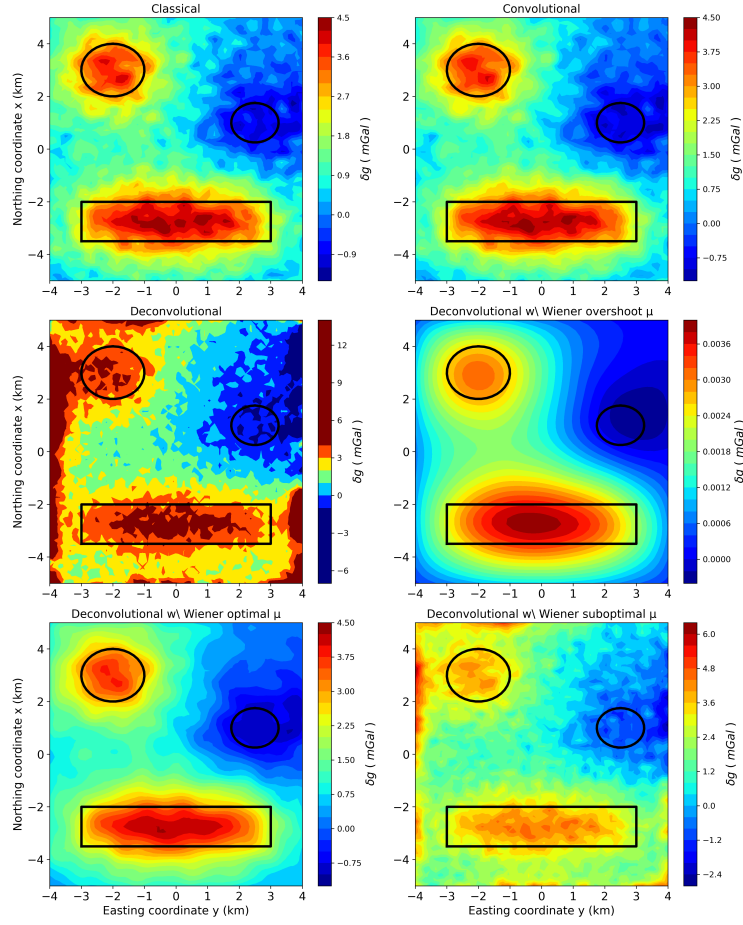


Figure 5. Predicted gravity data for different methods of the equivalent layer with maximum level of noise. Panel **(A)** is the classical method, **(B)** is the convolutional, **(C)** is the deconvolutional, **(D)** is the deconvolutional method using Wiener stabilization with a too high value for μ , **(E)** is the deconvolutional method using Wiener stabilization with a optimal value for μ and **(F)** is the deconvolutional method using Wiener stabilization with a too low value for μ .

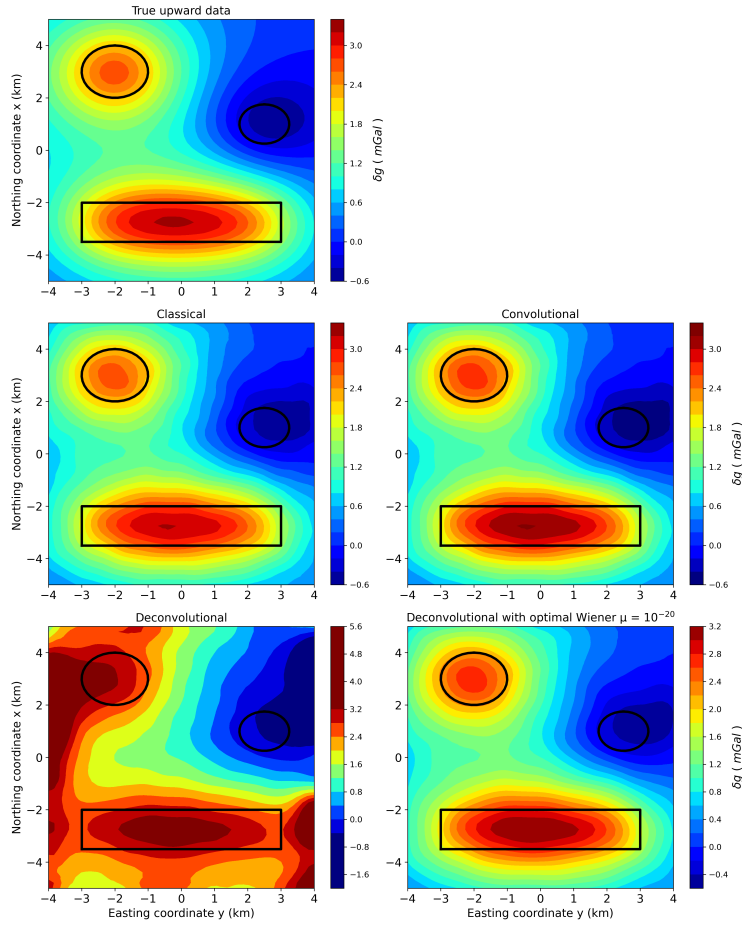


Figure 6. True noiseless upward gravimetric data at $z_i = -500$ m height and predicted data for different methods of the equivalent layer with maximum level of noise. Panel (A) is the true upward gravity data, Panel (B) is the classical method, (C) is the convolutional, (D) is the deconvolutional, (E) is the deconvolutional method using Wiener stabilization with a optimal value for $\mu = 10^{-20}$.

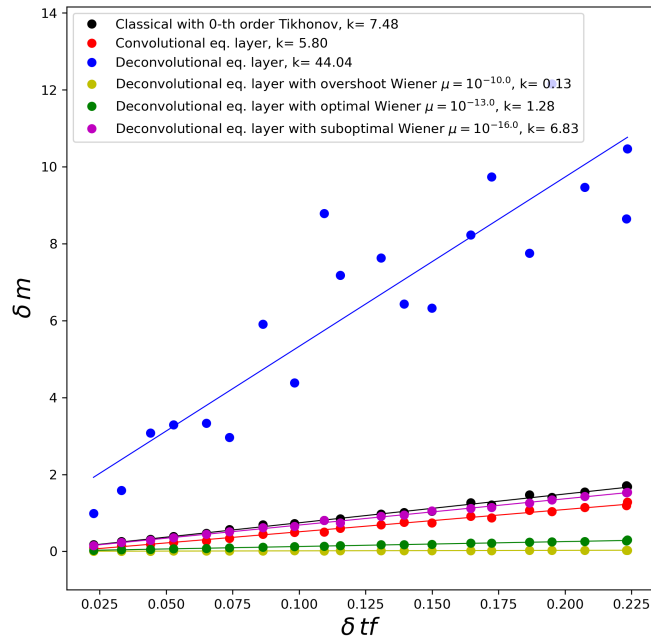


Figure 7. Stability analysis of some of the equivalent layer methods of the magnetic case.

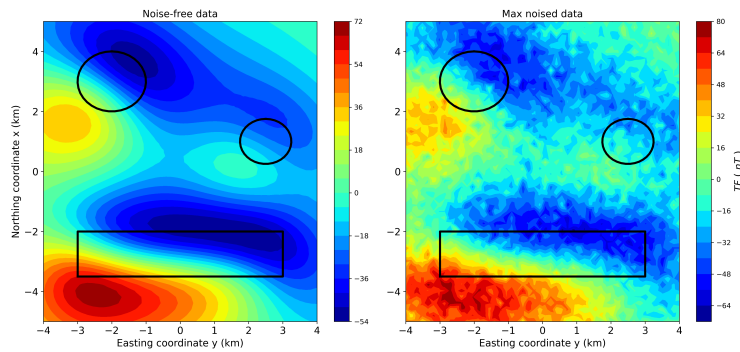


Figure 8. Synthetic data of the magnetic case. The observations points are placed in a regular grid of 50×50 . Panel (A) shows the noise-free data and panel (B) shows the maximum noised data (10%).

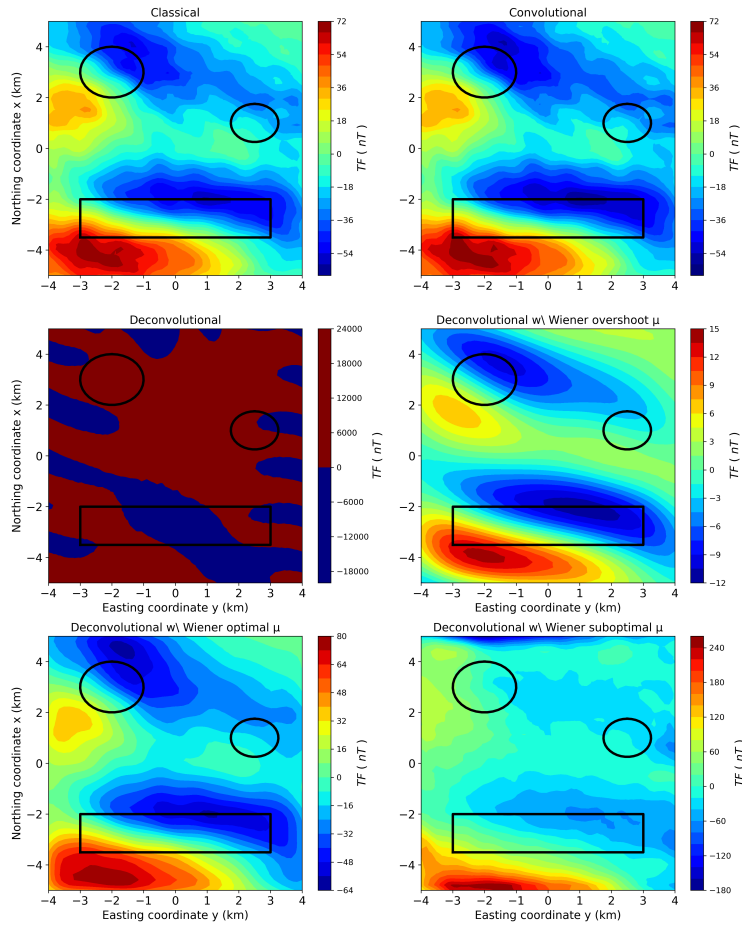


Figure 9. Predicted magnetic data for different methods of the equivalent layer with maximum level of noise. Panel **(A)** is the classical method, **(B)** is the convolutional, **(C)** is the deconvolutional, **(D)** is the deconvolutional method using Wiener stabilization with a too high value for μ , **(E)** is the deconvolutional method using Wiener stabilization with a optimal value for μ and **(F)** is the deconvolutional method using Wiener stabilization with a too low value for μ .

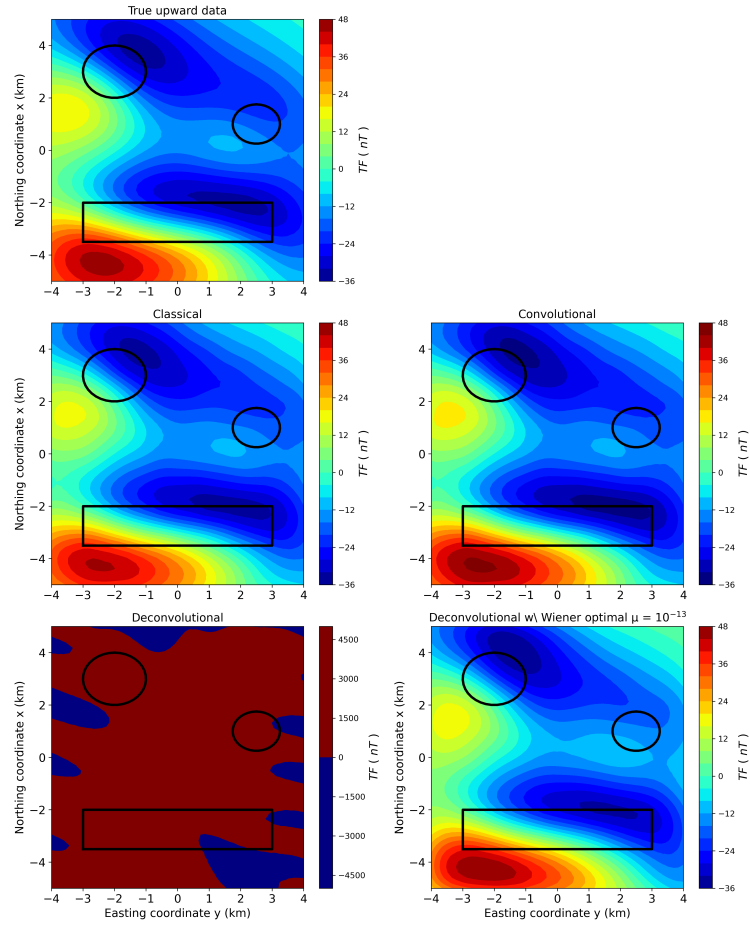


Figure 10. True noiseless upward magnetic data at $z_i = -1400$ m height and predicted data for different methods of the equivalent layer with maximum level of noise. Panel (A) is the true upward magnetic data, Panel (B) is the classical method, (C) is the convolutional, (D) is the deconvolutional, (E) is the deconvolutional method using Wiener stabilization with a optimal value for $\mu = 10^{-13}$.

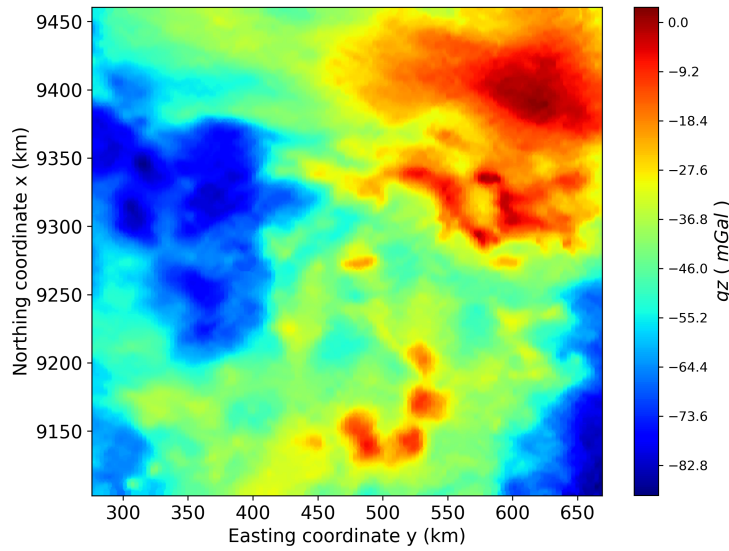


Figure 11. Gridded real aerogravimetric data from Carajás, Brazil. A regular grid of $1,000 \times 500$ is being used, totalizing $N, M = 500,000$ obsevation points and equivalent sources.

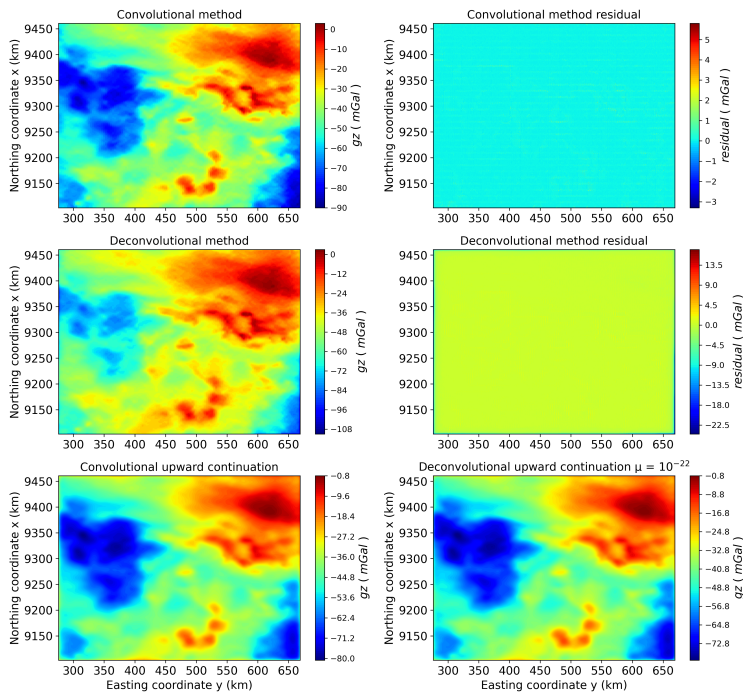


Figure 12. Panel (A) shows the Carajás predicted gravimetric data from convolutional equivalent layer method. Panel (B) shows the residual from the convolutional equivalent layer method. Panel (C) shows the predicted data from deconvolutional equivalent layer method. Panel (D) shows the residual from the deconvolutional equivalent layer method. Panel (E) shows the upward continuation at $z_i = -3500$ m for the convolutional method and Panel (F) shows the upward continuation at $z_i = -3500$ m for the deconvolutional method.

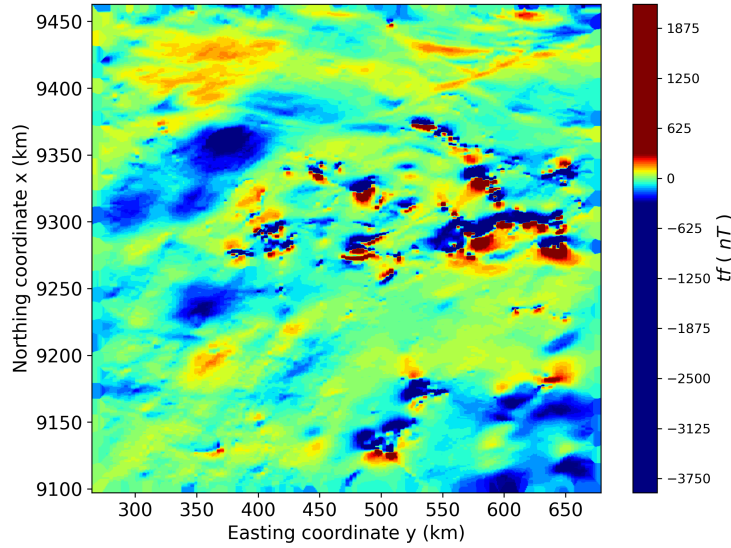


Figure 13. Gridded real aeromagnetic data from Carajás, Brazil. A regular grid of $1,000 \times 500$ is being used, totalizing $N, M = 500,000$ obsevation points and equivalent sources.

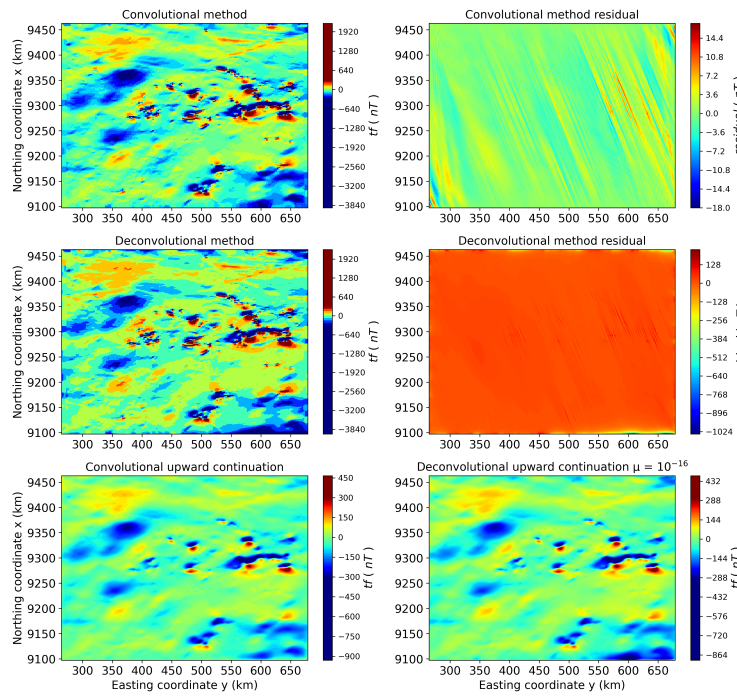


Figure 14. Panel (A) shows the Carajás predicted magnetic data from convolutional equivalent layer method. Panel (B) shows the residual from the convolutional equivalent layer method. Panel (C) shows the predicted data from deconvolutional equivalent layer method. Panel (D) shows the residual from the deconvolutional equivalent layer method. Panel (E) shows the upward continuation at $z_i = -3500$ m for the convolutional method and Panel (F) shows the upward continuation at $z_i = -3500$ m for the deconvolutional method.